Electronic Supplementary Information (ESI)

Interfacial effects in the inorganic/organic composite based on Bi_2Te_3 inducing decoupled transport properties and enhanced thermoelectric performance

Cham Kim*[a] , Jaehun Cho [a], Taewook Kim [b] and David Humberto Lopez [c]

[a] Daegu Gyeongbuk Institute of Science and Technology (DGIST), 333 Techno Jungang-daero, Daegu, 42988, Republic of Korea

[b] Department of Energy Chemical Engineering, Kyungpook National University, Sangju, 37224, Republic of Korea

[c] Department of Chemical and Environmental Engineering, University of Arizona, 1133 E. James. E. Rogers Way, Tucson, AZ, 85721, USA

Electronic Supplementary Information I

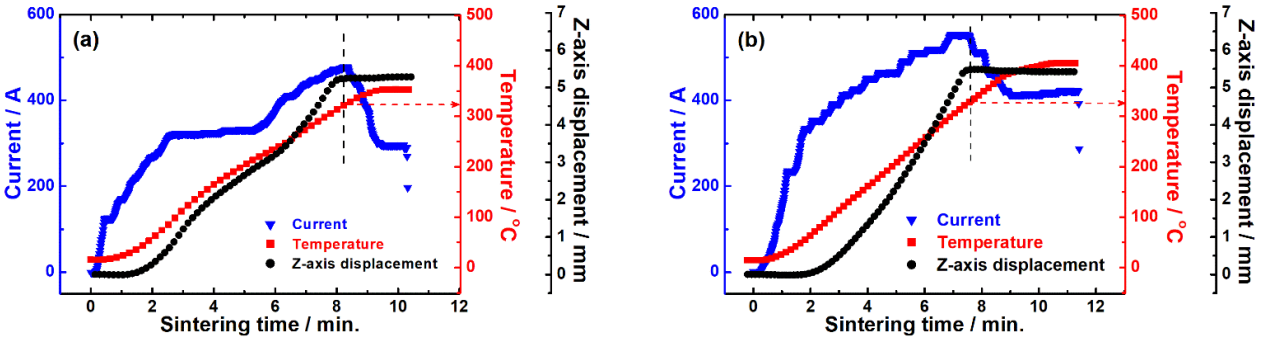

Figure S1. Variations in the Z-axis displacement of a graphite mold filled with the pristine Bi_2Te_3 during the spark plasma sintering process at 350 °C (a) and 400 °C (b).

The spark plasma sintering temperature is controlled by the electric current. When the temperature is elevated, the Z-axis displacement also increases (Figure S1), indicating that the Bi_2Te_3 in a graphite mold is compacted due to the temperature. The Z-axis displacement is observed to saturate at approximately 325 °C, which is possibly suggested as the lowest sintering temperature for the Bi_2Te_3.

The sintering temperature is elevated somewhat over 325 °C to guarantee that the sintering is completed; thus, the Bi_2Te_3 is individually reached to 350 °C (Figure S1a) and 400 °C (Figure S1b). These temperatures are maintained for 1 min under a pressure of 100 MPa in an Ar atmosphere, and thus cylindrical bulk specimens (12.0 mm × 13.8–14.1 mm ($d \times h$)) are finally obtained

Electronic Supplementary Information II

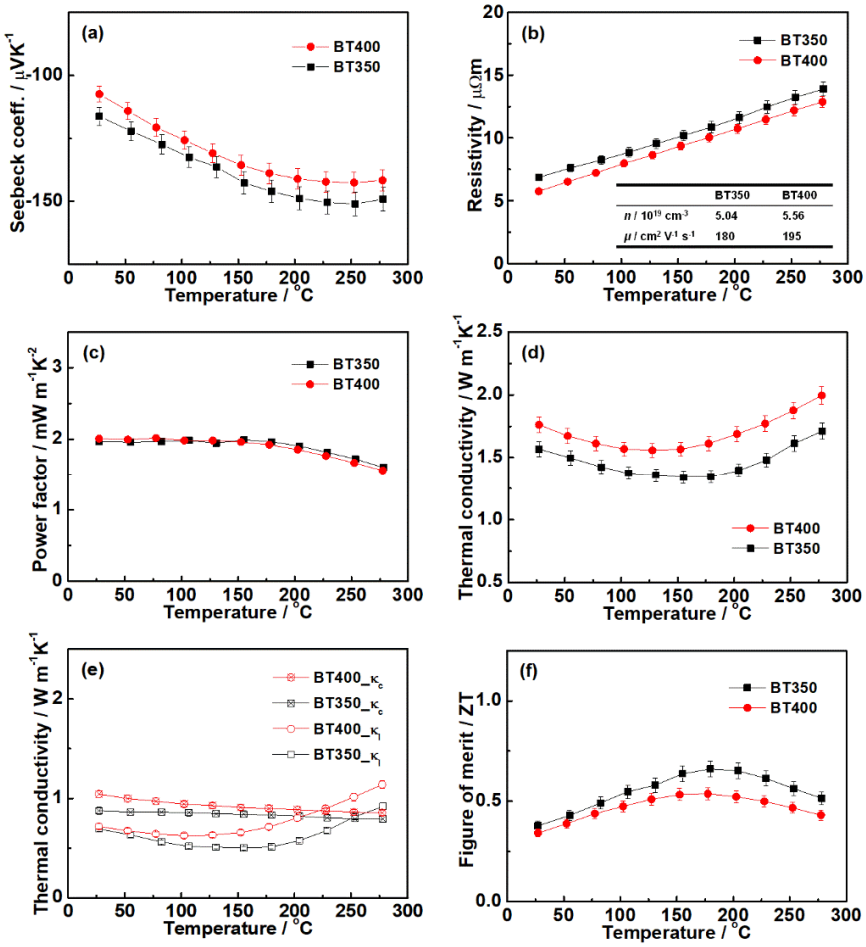

Figure S2. Thermoelectric transport properties of the pristine Bi_2Te_3 sintered at 350 °C and 400 °C: (a) Seebeck coefficient, (b) electrical resistivity, (c) power factor, (d) thermal conductivity divided into (e) carrier (κ_c) and lattice (κ_l) contributions, and (f) *ZT*. Error bars are shown when they exceed the symbol size.

The pristine Bi_2Te_3 sintered at 350 °C (BT350) exhibits higher Seebeck coefficient and electrical resistivity than that sintered at 400 °C (Figure S2a, S2b) because the former records lower carrier concentration and mobility than the latter (Figure S2b inlet). The variations in the Seebeck coefficient and electrical resistivity are canceled out, and thus they result in no considerable difference in the power factors of the BT350 and BT400 (Figure S2c). In addition, the BT350 exhibits lower thermal conductivity than the BT400 because the former has lower carrier and lattice thermal contributions than the latter (Figure S2e). Not only does the BT350 record the low carrier concentration/mobility but it may have low grain growth degree compared to the BT400; thus, the BT350 has the lower carrier and lattice thermal contributions. The BT350 records higher ZT than the BT400 (Figure S2f) due to the variation in the thermal conductivity rather than those in the electrical properties.

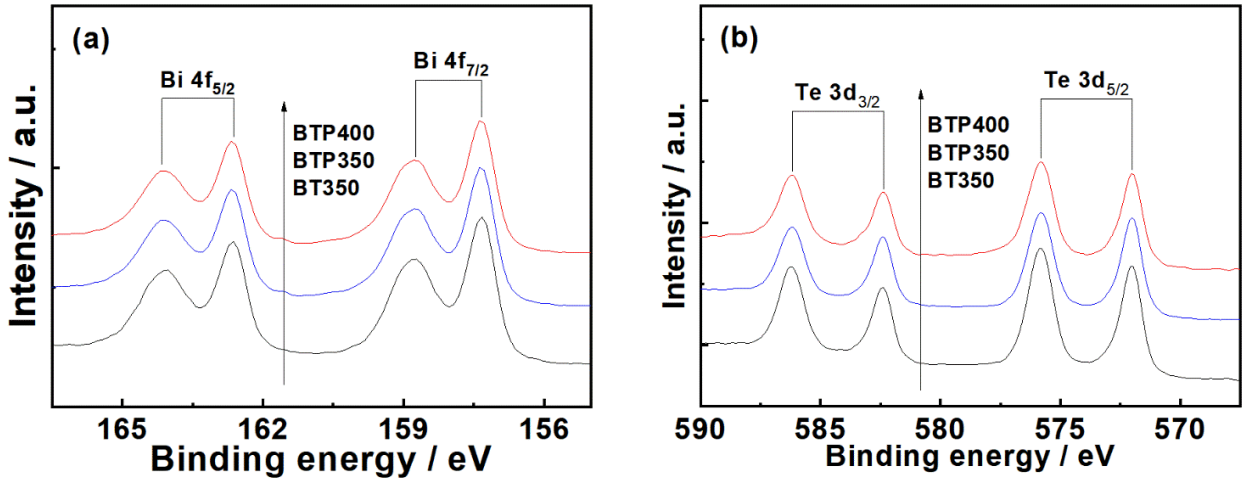

Figure S3. XPS spectra for Bi (a) and Te (b) of the Bi_2Te_3/PEDOT:PSS (BTP) composite and pristine Bi_2Te_3 (BT), which are sintered at 350 and 400 °C. Core levels of the spectra are presented as Bi 4f (a) and Te 3d (b), respectively.

The pristine Bi_2Te_3 exhibits the Bi 4f doublet signals of $4f_{5/2}$ and $4f_{7/2}$ in the high (165.0–162.0 eV) and low (159.8–156.5 eV) binding energy regions, respectively (Figure S3a). The Bi_2Te_3 also displays the Te 3d doublet signals of $3d_{3/2}$ and $3d_{5/2}$ in the binding energy regions of 587.7–581.2 eV and 577.5–570.9 eV, respectively (Figure S3b). The Bi_2Te_3/PEDOT:PSS composites show no significant changes in the signal shapes and binding energies of both Bi 4f and Te3d signals; thus, the Bi_2Te_3 may not react with any atomic components of the PEDOT:PSS while the composite is organized between the two components.

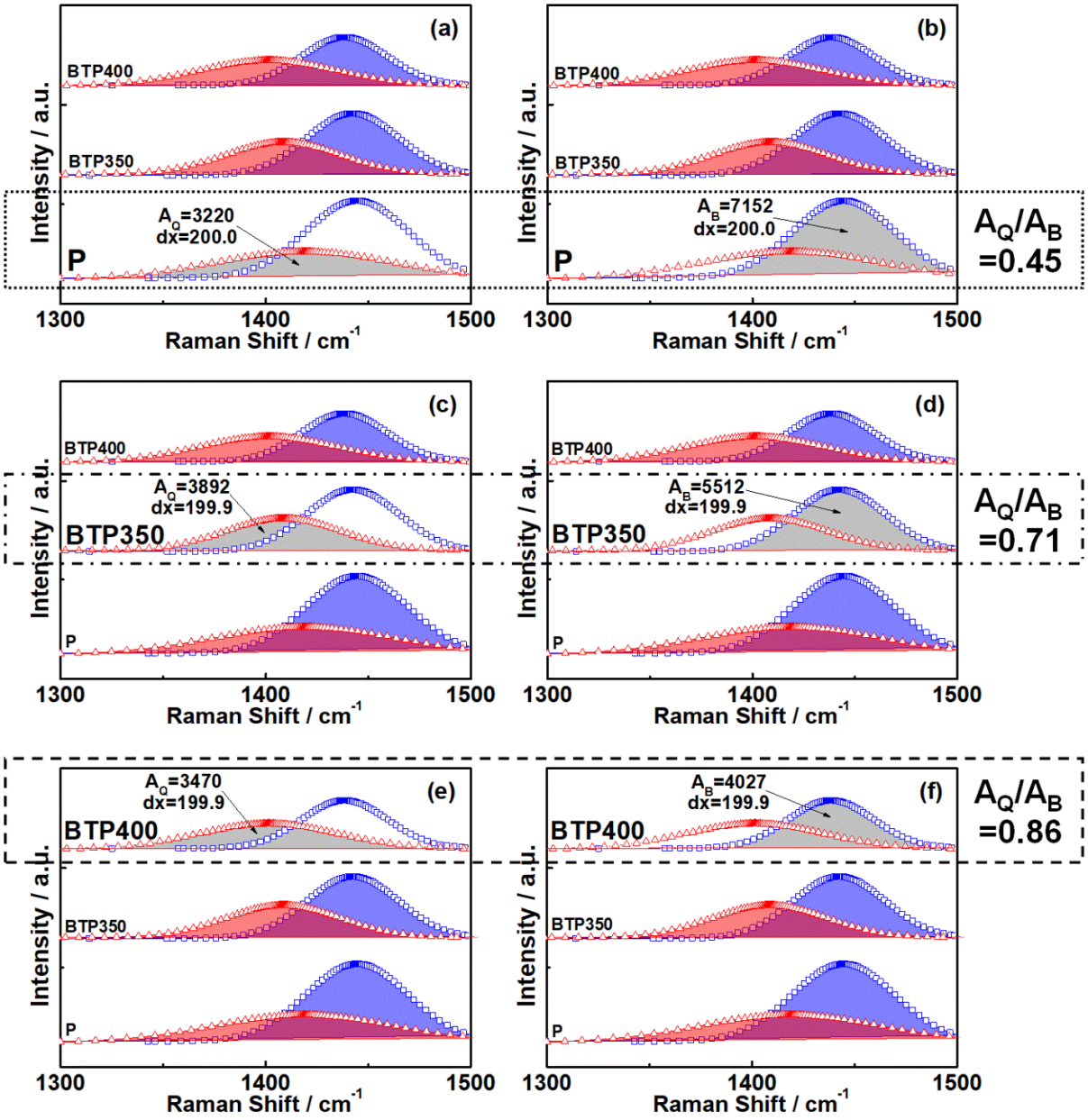

Figure S4. Raman spectra showing the C_{α}=C_{β} stretching vibrations in PEDOT thiophene rings for the pristine PEDOT:PSS (P; a,b) and Bi_2Te_3-PEDOT:PSS (BTP; c–f), which are identified as quinoid (Q; red spectrum) and benzoid (B; blue spectrum) signals of PEDOT. The spectrum areas (A; grey region) are derived by integrating each spectrum, and thus the area ratios (A_Q/A_B) are given for the samples.

Electronic Supplementary Information V

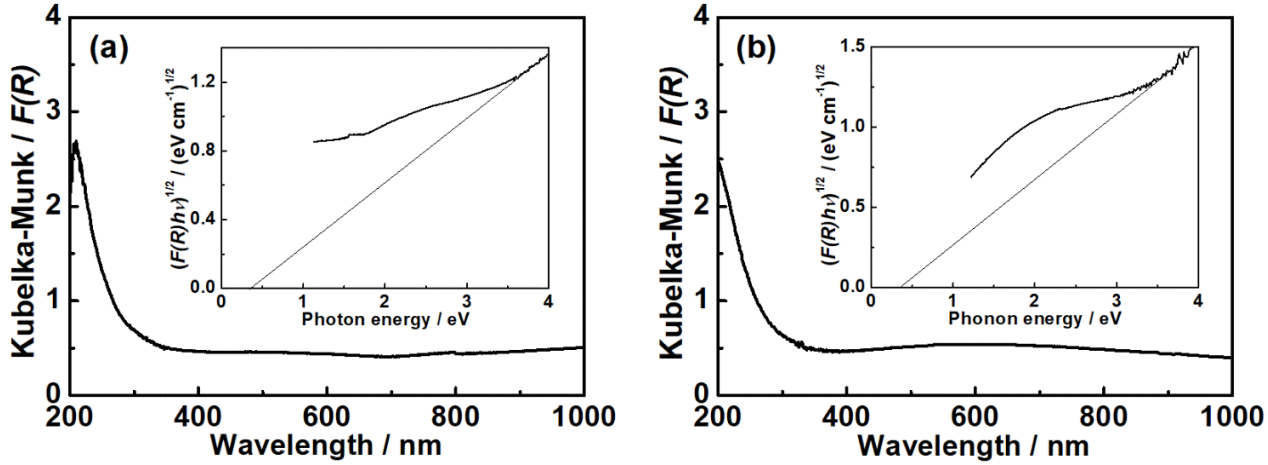

Figure S5. Kubelka-Munk functions (*F(R)*) of the Bi_2Te_3 sintered at 350 °C (a) and 400 °C (b), which are approximated using the reflectance (*R*) of the Bi_2Te_3, afford the optical absorbance of the Bi_2Te_3. Tauc plots of the Bi_2Te_3 using the Kubelka-Munk functions to derive the bandgap energies via least squares fitting (inlets).

To obtain the bandgap energy of the Bi_2Te_3 component, the Tauc plot is adopted as given below,

$$(F(R)hv)^{1/n} = A(hv - E_g)$$

where $F(R)$ is the Kubelka-Munk function, hv is the incident photon energy, n is the constant determined by the transition nature that a sample undergoes, A is the proportional constant, and E_g is the bandgap energy. The Kubelka-Munk function ($F(R) = (1–R)^2/2R$) allows the optical absorbance of the Bi_2Te_3 to be approximated from their diffuse reflectance (R). The n values are 1/2, 3/2, 2, and 3 for direct allowed, direct forbidden, indirect allowed, and indirect forbidden transitions, respectively. Bi_2Te_3 has an indirect bandgap, which shows allowed transition, and thus 2 is selected as the n value. We generate the plot of $(F(R)hv)^{1/n}$ versus hv and found the bandgap energy of the Bi_2Te_3 using a least-square fit (inlets).

Electronic Supplementary Information VI

Table S1. *ZT* values (*ZT* maximum: ZT_{max}, *ZT* average: ZT_{ave} at 50–150 °C) of the Bi_2Te_3-PEDOT:PSS (BTP) compared to those of previously reported binary (Bi_2Te_3) and ternary ($Bi_2(Te,Se)_3$, $Bi_2(Te,I)_3$) compounds.[1-5]

	BT-P	Bi_2Te_3 nanosheet[1]	Bi_2Te_3 nanostructure[2]	$Bi_2Te_{2.5}Se_{0.5}$ nanostructure[3]	$Bi_2Te_{2.7}Se_{0.3}$ nanoplate[4]	$Bi_2Te_{2.9}I_{0.1}$ nanoparticle[5]
ZT_{max}	1.19 (132 °C)	1.16 (150 °C)	0.88 (127 °C)	1.18 (190 °C)	1.10 (120 °C)	1.10 (175 °C)
ZT_{ave} (50–150 °C)	1.14	1.00	0.84	0.94	0.93	0.91

The Bi_2Te_3-PEDOT:PSS (BTP) records the ZT_{max} and ZT_{ave} values of 1.19 at 132 °C and 1.14 at 50–150 °C, respectively. Compared to the binary and ternary n-type equivalents recently reported, the Bi_2Te_3-PEDOT:PSS shows similar ZT_{max} value but it exhibits higher ZT_{ave} value than the equivalents by 14–23%. Considering the superior ZT_{ave} value at 50–150 °C, the Bi_2Te_3-PEDOT:PSS is anticipated to be highly applicable to the promising thermoelectric generations at low temperatures, such as energy harvesting devices and systems.

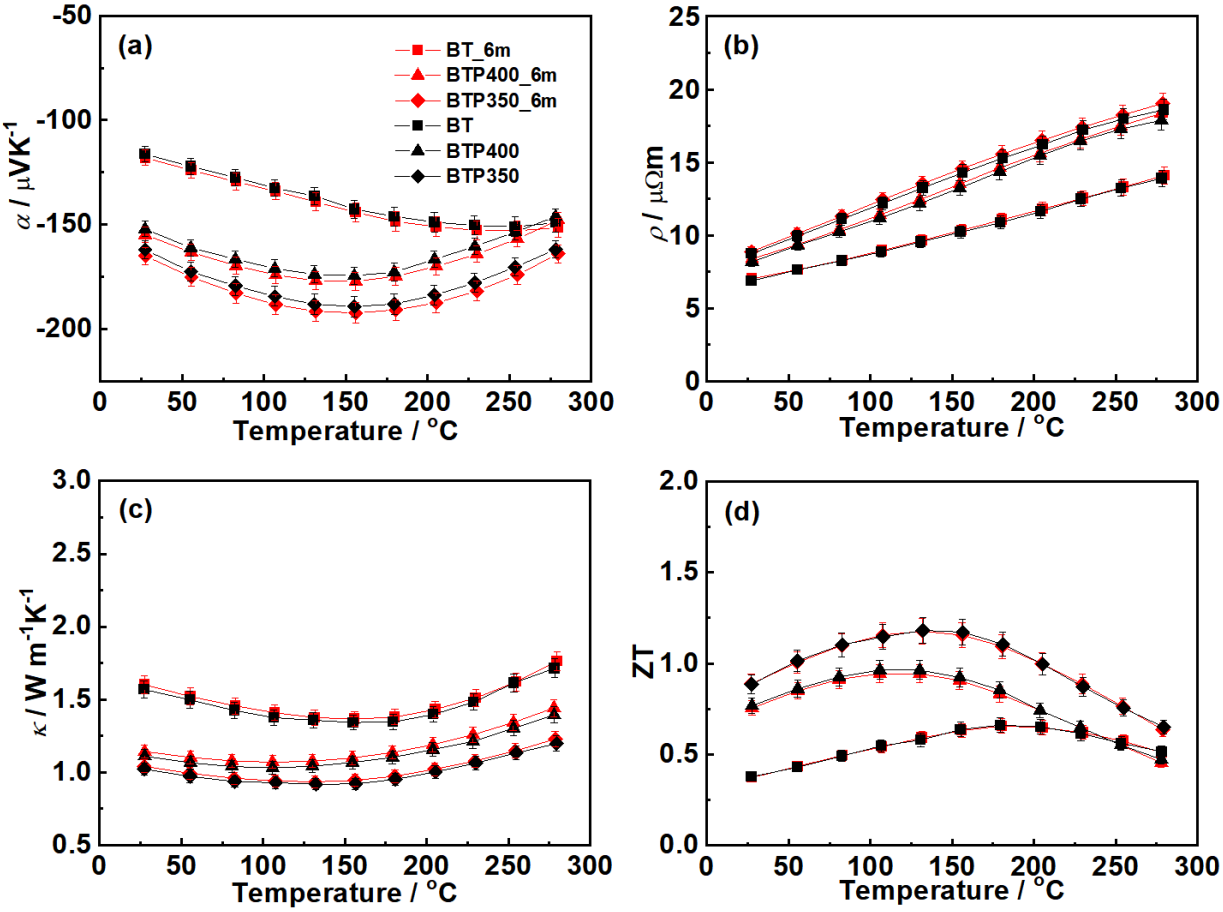

Figure S7. Thermoelectric transport properties of the Bi_2Te_3-PEDOT:PSS (BTP) and pristine Bi_2Te_3 (BT), which are six months old (marked as red colors): (a) Seebeck coefficient (α), (b) electrical resistivity (ρ), (c) thermal conductivity (κ), and (d) ZT. The thermoelectric transport properties are compared to those in Figure 6. Error bars are shown when they exceed the symbol size.

After measuring the thermoelectric transport properties of the Bi_2Te_3-PEDOT:PSS and pristine Bi_2Te_3 (Figure 6), we left the samples in ambient conditions for about six months and measured the properties again (red colors in Figure S7). It is observed that all of the values exist within the measurement error ranges.

References

1 F. Wu, H. Song, F. Gao, W. Shi, J. Jia and X. Hu, *J. Electron. Mater.*, 2013, **42**, 1140.

2 L. Yang, Z. G. Chen, M. Hong, G. Han and J. Zou, *ACS Appl. Mater. Interfaces*, 2015, **7**, 23694.

3 B. Xu, T. Feng, M. T. Agne, L. Zhou, X. Ruan, G. J. Snyder and Y. Wu, *Angew. Chem.*, 2017, **56**, 3546.

4 M. Hong, T. Chasapis, Z. G. Chen, L. Yang, M. G. Kanatzidis, G. J. Snyder and J. Zou, *ACS Nano*, 2016, **10**, 4719.

5 F. Wu, W. Wang, X. Hu and M. Tang, *Prog. Nat. Sci.*, 2017, **27**, 203.